ACS NANO
Cite This: ACS Nano 2018, 12, 6938–6948
www.acsnano.org

ARTICLE

Fluorinated Gold Nanoparticles for Nanostructure Imaging Mass Spectrometry

Amelia Palermo,[†,#] Erica M. Forsberg,[‡,#] Benedikt Warth,[§] Aries E. Aisporna,[†] Elizabeth Billings,[†] Ellen Kuang,[‡] H. Paul Benton,[†] David Berry,[∥] and Gary Siuzdak*[,†,⊥]

[†]Scripps Center for Metabolomics, The Scripps Research Institute, 10550 North Torrey Pines Road, La Jolla, California 92037, United States

[‡]Department of Chemistry and Biochemistry, San Diego State University, 5500 Campanile Drive, San Diego, California 92182, United States

[§]Department of Food Chemistry and Toxicology, Faculty of Chemistry and Vienna Metabolomics Center (VIME), University of Vienna, Währingerstraße 38, 1090 Vienna, Austria

[∥]Department of Microbiology and Ecosystem Science, Division of Microbial Ecology, Research Network Chemistry Meets Microbiology, University of Vienna, Althanstraße 14, 1090 Vienna, Austria

[⊥]Department of Chemistry, Molecular and Computational Biology, The Scripps Research Institute, 10550 North Torrey Pines Road, La Jolla, California 92037, United States

Supporting Information

ABSTRACT: **Nanostructure imaging mass spectrometry (NIMS) with fluorinated gold nanoparticles (f-AuNPs) is a nanoparticle assisted laser desorption/ionization approach that requires low laser energy and has demonstrated high sensitivity. Here we describe NIMS with f-AuNPs for the comprehensive analysis of metabolites in biological tissues. F-AuNPs assist in desorption/ionization by laser-induced release of the fluorocarbon chains with minimal background noise. Since the energy barrier required to release the fluorocarbons from the AuNPs is minimal, the energy of the laser is maintained in the low μJ/pulse range, thus limiting metabolite in-source fragmentation. Electron microscopy analysis of tissue samples after f-AuNP NIMS shows a distinct "raising" of the surface as compared to matrix assisted laser desorption ionization ablation, indicative of a gentle desorption mechanism aiding in the generation of intact molecular ions. Moreover, the use of perfluorohexane to distribute the f-AuNPs on the tissue creates a hydrophobic environment minimizing metabolite solubilization and spatial dislocation. The transfer of the energy from the incident laser to the analytes through the release of the fluorocarbon chains similarly enhances the desorption/ionization of metabolites of different chemical nature, resulting in heterogeneous metabolome coverage. We performed the approach in a comparative study of the colon of mice exposed to three different diets. F-AuNP NIMS allows the direct detection of carbohydrates, lipids, bile acids, sulfur metabolites, amino acids, nucleotide precursors as well as other small molecules of varied biological origins. Ultimately, the diversified molecular coverage obtained provides a broad picture of a tissue's metabolic organization.**

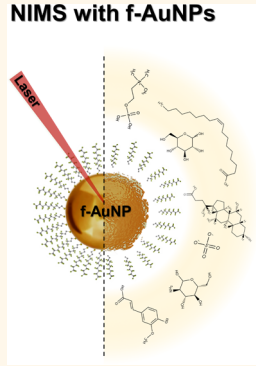

KEYWORDS: *nanostructure imaging mass spectrometry, perfluorinated gold nanoparticles, mass spectrometry imaging, metabolomics, gut microbiome, mice, fiber free diet*

Mass spectrometry imaging (MSI) was designed to detect and spatially localize molecules on surfaces.[1−4] Many MSI strategies have been proposed, of which currently the most employed is matrix-assisted laser desorption ionization (MALDI) coupled to time-of-flight mass spectrometry (TOF-MS).[5,6] This approach leverages the cocrystallization of the sample with a highly volatile UV-adsorbing matrix, usually sinapinic acid (SA), α-cyano-4-hydroxycinnamic acid (CHCA), or 2,5-dihydroxybenzoic acid (DHB), which transfers the energy from an incident laser beam to the analytes,[7,8] thus aiding the soft ionization and desorption of analyte molecules.

MALDI-MS can provide high throughput analysis; however, its application for comparative metabolomics MSI studies, for example in systems biology or personalized medicine, remains limited.[9−11] This is primarily due to signal variability stemming from the uneven formation of the matrix-analyte crystals in so-called "sweet spots",[12] and little ionization consistency for molecules of diverse chemical nature.[13] Moreover, the

Received: March 29, 2018
Accepted: July 2, 2018
Published: July 2, 2018

DOI: 10.1021/acsnano.8b02376
ACS Nano 2018, 12, 6938–6948

generation of background ions from the matrix can interfere with the detection of low molecular weight molecules (m/z < 700 Da), including metabolites and drugs.[13,14] Although a more even crystallization of the matrix on the surface of the sample can be achieved by sublimation,[15,16] the noise deriving from the ionization of the matrix significantly suppresses the detection of small molecules, thus complicating the application of MALDI for comparative global metabolomics and pharmaceutical studies.

Over the last two decades, several efforts have been made to minimize MALDI background interference, leading to the further development of existing matrix-free secondary ion mass spectrometry (SIMS), and multiple new approaches including desorption electrospray ionization (DESI), laser ablation electrospray ionization (LAESI),[17] and nanostructure imaging mass spectrometry (NIMS).[5,18] SIMS desorbs and ionizes the analyte by focusing an ion beam on the surface of the sample, typically a collated primary high-energy atomic ion beam of Ga^+, Cs^+, O_2^+, or a ion cluster beam of C_{60}^+, Au_3^+, Ar_{2500}^+ or Bi_3^+.[19−21] While the use of an atomic ion beam calls for a trade-off between spatial resolution and in source fragmentation events and generates complex spectra,[5,20] the use of a cluster ion beam (cluster projectiles) significantly reduces this issue.[22,23] For example, SIMS with argon gas clusters has been successfully applied for 2- and 3-dimensional in depth profiling of drugs and metabolites at single cell level with exquisitely high spatial resolution (up to 10−100 nm).[24−26] However, it remains unknown whether the approach covers the detection of central carbon metabolites, which are of key relevance in metabolomics studies. Additionally, by using large clusters such as Ar_{2500}^+ the desorption can be very efficient, however the ionization less so, as well as the use of high lateral resolution may bias the detection toward the most abundant and easily ionizable molecules in the sample (*e.g.*, lipids in biological tissues).

DESI is characterized by a very soft desorption/ionization (D/I)[27] operated under ambient conditions where a sample can be directly analyzed without any prior preparation. A stream of charged solvent droplets are electrosprayed directly onto the sample surface, solvating and liberating the analytes as gaseous ions that are then focused into the mass spectrometer.[28] DESI allows for real-time monitoring of biological and industrial processes.[29,30] However, ambient conditions are not always desirable as they are often incompatible with the stability of the analyte toward, for example, oxidation, and metabolic biotransformations may occur after sampling. Furthermore, the use of droplets limits the spatial resolution and requires the optimization of the solvent depending on the specific type of sample and targeted molecules.[31]

NIMS is an alternative approach for surface assisted laser desorption ionization (SALDI) of small molecules and metabolites[18] also applied to MSI.[32−35] It originally employed etched porous silicon surfaces nanostructured with a thin layer of an initiator molecule (*e.g.*, heptadodecafluoro-1,1,2,2-tetrahydrodecyl-tetramethyldisiloxane). In the resulting clathrate structures, the energy is transferred from the incident laser to the initiator, which is vaporized from the surface, thus facilitating the D/I of the analytes. This approach can also be coupled with SIMS ion sources using, for example, Bi_3^+ or Ga^+ ion beams (nano-NIMS),[18] thus offering the possibility to reach lateral resolution on the nanometer scale. However, the classic NIMS protocol involves the use of hydrofluoric acid (HF), an extremely hazardous chemical that can be handled only under special safety protocols in certified laboratories. We have therefore recently developed an improved approach for NIMS based on functionalized gold nanoparticles (f-AuNPs).[36]

Different types of carbon, silica or metal nanostructured surfaces and nanoparticles have been previously employed for the enhancement of the D/I of small molecules and lipids, as these can offer extended dynamic ranges thanks to the ample surface area and efficient energy transfer properties combined with reduced background noise.[13,37−44] Among these, AuNPs are particularly appealing for MSI because of their biocompatibility and interesting physical properties.[45] For instance, bare AuNPs have been applied for the D/I of carbohydrates[46] and amino acids,[47] aminothiols,[48] fatty acids and nucleobases,[46] or for the selective detection of glutathione.[49] Despite these benefits, AuNPs require high laser energies for the D/I of metabolites, with associated laser-induced fragmentation as well as adsorption of metabolites at the NP surface.[36,37,50] These limitations have prevented their widespread application for the simultaneous detection of a broad range of metabolites in space.

By contrast, the use of AuNPs functionalized with perfluorinated chains allows the use of lower laser energies due to a mostly kinetic D/I enhancement effect (release of the fluorocarbons chains), which prevents the direct contact of the analyte with the thermal energy at the AuNP surface.[37] Moreover, the nonadherent nature of the perfluorinated layer on the surface of the particle impedes the selective adsorption of metabolites, making the approach amenable to the detection of a broad range of metabolites and small molecules.

Since the first implementation and application of f-AuNPs as a versatile approach for multimodal molecular imaging of biological specimens by MSI, X-ray and electron microscopy with breathable liquids,[36] this technology has been further characterized becoming a powerful tool for metabolomics MSI directly from the surface of biological tissues, requiring minimal sample preparation while providing low background interference and minimal metabolite dislocation. This approach can be considered an advanced method of nanoparticle assisted laser desorption ionization (nano-PALDI), which leverages the NIMS concept by using nanostructured nanoparticles as initiators of the D/I process.

Here, we present NIMS with f-AuNPs for the targeted and untargeted analysis of metabolites from biological tissues. We further assess the applicability of the approach for comparative untargeted metabolomics MSI studies by exploring variations occurring in the mouse colon under different diet regimens.

NIMS with f-AuNPs permits heterogeneous molecular coverage, allowing the direct detection of carbohydrates, lipids, bile acids, sulfur metabolites, amino acids, nucleotide precursors as well as other small molecules of biological origin with high sensitivity and minimal metabolite dislocation in space.

RESULTS AND DISCUSSION

f-AuNPs for Metabolomics NIMS. AuNPs can be functionalized with a variety of ligands by performing gold−thiol reactions with straightforward synthetic protocols.[51−53] For NIMS, we functionalized the surface of octanethiol AuNPs with 1*H*,1*H*,2*H*,2*H*-perfluorodecanethiol chains *via* dithiol coupling in a one-step reaction.[36] This led to the formation of a highly ordered perfluorinated nanostructured monolayer

DOI: 10.1021/acsnano.8b02376
ACS Nano 2018, 12, 6938−6948

on the surface of the AuNPs (Figure 1A), which allows the translation of the NIMS technology directly on the surface of the AuNPs without the use of the hazardous HF.

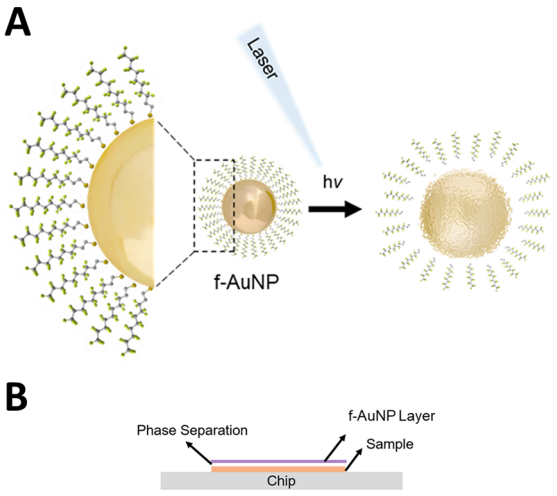

Figure 1. (A) Schematic of the perfluorinated monolayer on the surface of the f-AuNP. When the laser hits the nanoparticle, the energy is transferred to the surface causing the thermal release of the fluorinated chains. (B) Phase separation between the f-AuNPs dissolved in perfluorohexane and the surface of the sample.

The formation of the perfluorocarbon layer on the AuNP provides several advantages for the detection of metabolites and other small molecules in biological tissues. First, the resulting highly hydrophobic f-AuNPs can be solubilized in the biocompatible and water-repellent solvent perfluorohexane (PFH).[54] The topical distribution of the f-AuNPs dissolved in PFH creates a nonadherent film, which remains distinctly separate from the hydrophilic surface of the sample (*e.g.*, tissues, cell extracts) (Figure 1B). This aspect is of key relevance as it prevents the solubilization and spatial dislocation of the analytes (Figure S1), thus enabling NIMS of metabolites at a resolution only limited by the laser spot size. For example, by further optimization of the geometry of the laser source, as recently reported by Kompauer *et al.*,[2] the D/I may be operated at smaller laser diameters (higher lateral resolution) without reducing the incident energy. Moreover, PFH is a stable, nonreactive and highly volatile solvent,[55] which spontaneously and rapidly vaporizes from the surface of the sample after uniform distribution of the f-AuNPs, without chemical modification of the analytes (Figure 1B).

For analyte D/I, f-AuNPs function similarly to NIMS with porous silicon containing initiators by providing a highly structured surface for efficient energy transfer and facile analyte desorption. When the laser light hits the f-AuNPs, the energy absorbed by the gold nanoparticle is transferred to the surface where it cleaves the disulfide bonds (Figure 1A). The release of the fluorinated chains further promotes the desorption of the analytes from the surface of the sample.[36] Interestingly, a portion of the laser energy is transformed into thermal energy, as shown by the apparent melting of the f-AuNPs to form larger particles in transmission electron microscopy (TEM) images of the f-AuNPs after laser irradiation (Figure 2A). Since the diameter of the f-AuNPs is on the order of nanometers, the morphology of the tissue is also preserved during the desorption process (Figure 2B).

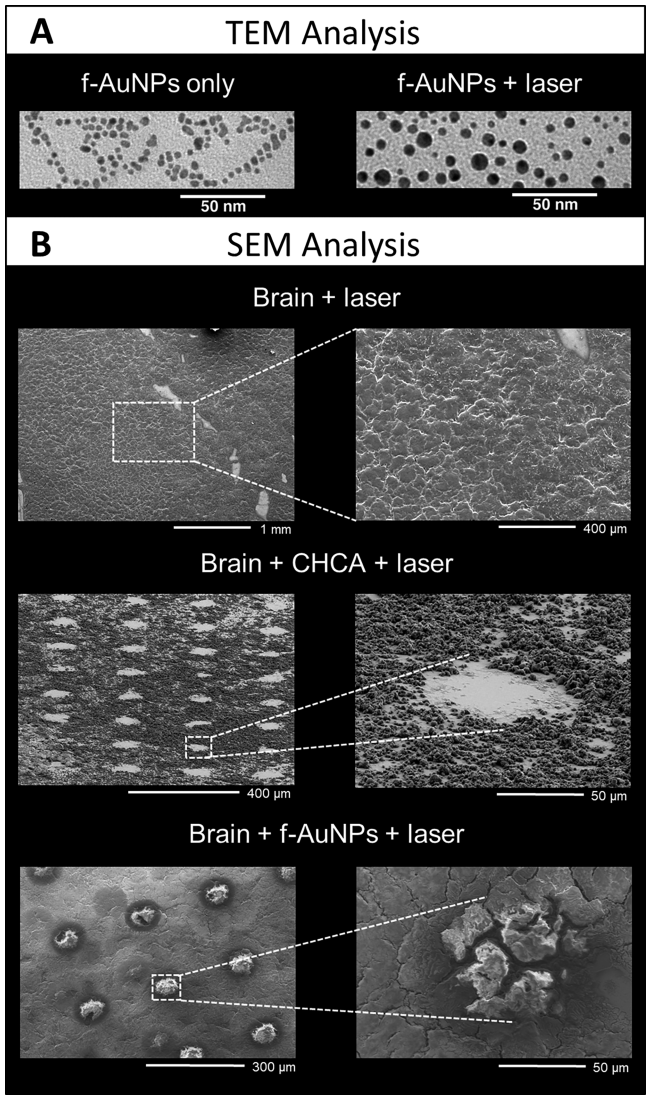

Figure 2. (A) TEM images of f-AuNPs before and after laser irradiation. (B) SEM images obtained after laser irradiation of mouse brain tissue only, mouse brain tissue with α-cyano-hydroxycinnamic acid (CHCA) matrix, and mouse brain tissue with f-AuNPs.

Another benefit of using f-AuNPs for NIMS is linked to the low energy required for cleavage of the disulfide bonds,[36] which enables the use of relatively low laser energy (μJ/pulse range). This limits in-source fragmentation events and thermal degradation of labile analytes.[36] Scanning electron microscopy analysis (SEM) of brain tissue surfaces after MALDI and f-AuNP NIMS, shows a distinct "raising" of the tissue surfaces as compared to MALDI ablation (Figure 2B). This is associated with the low laser energy and the likely release of water vapor, supporting a more gentle D/I mechanism which aids in the generation of intact molecular ions. Therefore, f-AuNPs promote a softer form of LDI at lower laser energies when compared to bare AuNPs.[36,37] Bare AuNPs primarily leverage a thermally driven D/I mechanism prone to analyte in-source fragmentation and the generation of metal cluster ions. Moreover, the fluorinated surface of the f-AuNPs prevents chemical and physical interactions that may occur between the surface of the AuNP and the metabolites.[37]

DOI: 10.1021/acsnano.8b02376
ACS Nano 2018, 12, 6938–6948

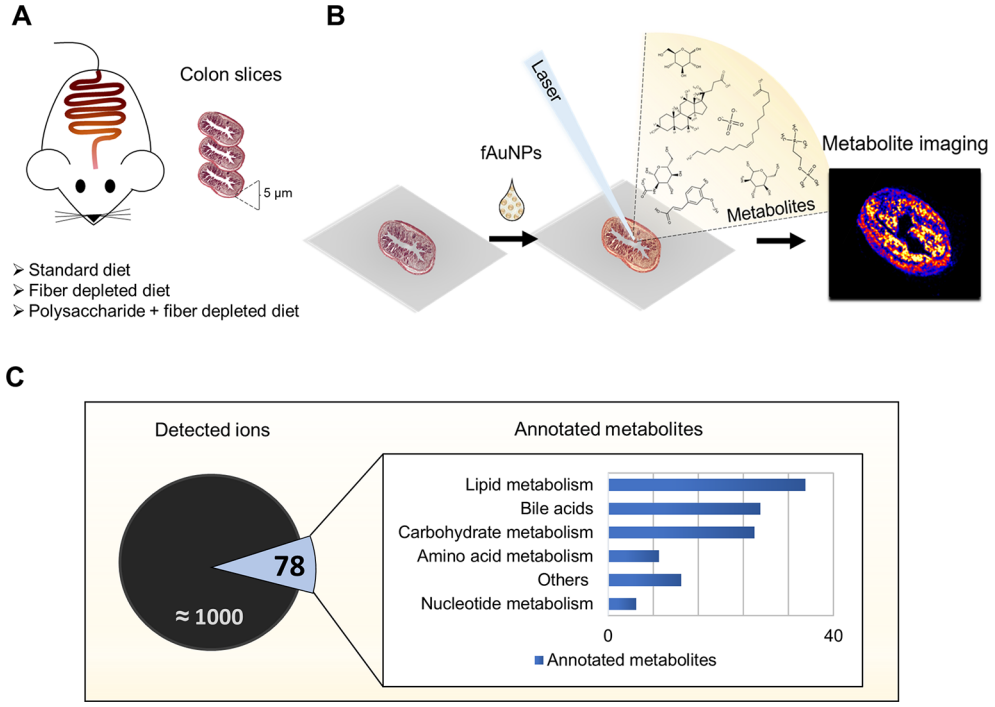

Figure 3. (A) Schematic of the *in vivo* study. (B) f-AuNPs NIMS workflow for metabolite imaging in mouse colon samples. (C) number of detected features *vs* annotated metabolites obtained in the analysis of 5 μm mouse colon slices. Mice were fed with standard diet and metabolome coverage is reported for each chemical class.

Compared with other approaches, the absence of the analyte-matrix cocrystallization step, together with the uniform distribution of the f-AuNPs on the sample and the reduced laser energy required for the D/I, allow increased reproducibility and reduced matrix interference. Interestingly, since the f-AuNP solution in PFH possesses both hydrophobic and lipophobic behavior, the D/I enhancement effect can be coupled to the use of other matrices for nanoscaping—the selective preconcentration of the analytes in the sample—without interference. For example, anion exchange resin nanoparticles (*e.g.*, Dowex) can be used to selectively enhance the signal detected from cell extracts through a pretreatment step (Figure S2).

Altogether these aspects make f-AuNPs a viable and versatile solution for MSI of metabolites in biological tissues, offering high throughput detection of small molecules (<700 Da) combined with the excellent sensitivity and minimal background noise of NIMS.[18]

f-AuNPs for Metabolomics NIMS of the Mouse Colon. Currently available methods for imaging metabolites provide limited coverage in the low molecular mass range (MW < 700 Da) and are generally biased toward the detection of the most abundant, easily ionizable lipids.[56] To address this, we explored NIMS with f-AuNPs for the detection of different classes of metabolites and assessed its applicability by performing the approach for the targeted and global exploration of the metabolic content of the mouse colon (Figure 3A). Fresh frozen samples obtained from control mice fed with the standard diet were embedded in optimal cutting temperature compound (OCT) and cut to obtain 5 μm tissue sections. Each slice was then transferred onto the surface of a clean piranha etched p-doped silicon chip and covered with the f-AuNPs solution in PFH (3 mg/mL) (Figure 3B). The chip was kept in a desiccator at room temperature until direct analysis using a Q-TOF MS system equipped with a MALDI source. Analytes were detected by high-resolution measurements in the 25−700 m/z range in full scan positive acquisition mode. Laser energy was optimized to reduce in source fragmentation and to avoid the generation of gold clusters while promoting D/I of metabolites at 30 μm lateral resolution. The obtained m/z list was putatively annotated against the METLIN database[57] using an in-house script (±5 ppm error, considering the $[M + H]^+$ and $[M - H_2O + H]^+$ ions and the $[M + Na]^+$ and $[M + K]^+$ adducts). Metabolite identities were confirmed by the presence of the M + 1 and M + 2 isotopic peaks and other related adducts with consistent spatial distribution, and by performing MS/MS experiments when possible. Phosphocholine ($[M + H]^+$, 184.0733 m/z) was used for tissue alignment.

Overall, our approach allowed for the global profiling and mapping of approximately 1000 features, and consistent annotation of approximately 80 metabolites distributed over six chemically diverse groups (Figure 3C, Table S1). Due to the absence of chromatographic separation in MSI experiments, isobaric compounds were detected as sum of intensities. Although metabolite dislocation in the gut tissue can be excluded due to the use of the nonadherent f-AuNPs in PFH as D/I matrix, attention has to be paid in colon tissue slicing/handling since slight metabolite displacements may occur in the colon lumen due to the absence of an organized tissue structure.

As expected, our data show that lipids are the most abundant class among the detected metabolites, followed by the bile acids. More interestingly, the approach also enabled the detection of highly hydrophilic compounds as to provide coverage for the central carbon metabolism, including carbohydrates, amino acids, nucleotides and a variety of related precursors (Figure 3C, Figure S3, Table S1). For

DOI: 10.1021/acsnano.8b02376
ACS Nano 2018, 12, 6938−6948

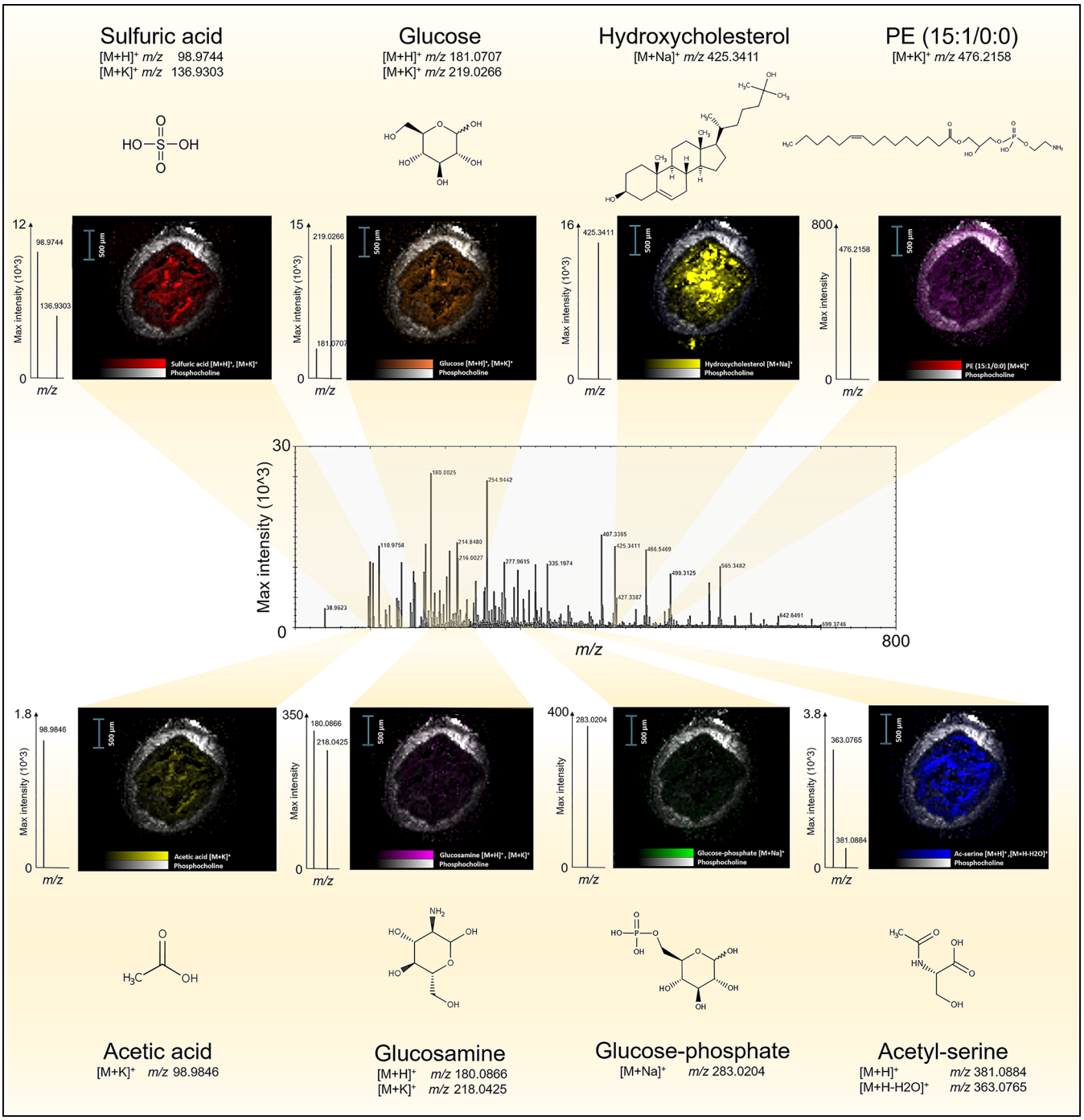

Figure 4. Mass spectrum obtained by f-AuNPs NIMS of a 5 μm mouse colon tissue slice. The insets show the distribution of targeted metabolites in the mice colon. Ion abundances were normalized according to the total signal in each pixel, and phosphocholine was used for tissue alignment.

example, glucose can be targeted as its stable $[M + K]^+$ adduct, or hydrocholesterol as its $[M + Na]^+$ adduct (Figure 4, Table S1). Matrix interference (*e.g.*, gold clusters) in the low m/z range is very limited due to the low laser energy employed and does not compromise the detection of low molecular weight metabolites.[36]

It is also worth noting that while attempting to understand metabolic dysregulations at a systems level, under certain conditions the activation or down regulation of a specific metabolic pathway can be inferred by measuring the abundance of few representative metabolites, used as proxy for the activity of the pathway.[58−60] Combining this observation with the highly heterogeneous metabolome coverage provided by the use of NIMS with f-AuNPs, we believe that this approach enables the comprehensive interpretation of metabolism with spatial resolution at a system level.

In addition to metabolites of murine origin, several bacterial metabolites were also detected in the colon samples (Table S1). For example, butyrate and acetate were detected as $[M + H]^+$ and $[M + K]^+$ ions. The interplay between these microbial metabolites and the mucosa/epithelial cells of the gut has

DOI: 10.1021/acsnano.8b02376
ACS Nano 2018, 12, 6938−6948

recently raised substantial interest, particularly with several observed correlations with human processes. For example, butyrate has been found to play a key role in the regulation of stem cell differentiation.[61]

In this context, our approach represents an advantageous tool for disentangling the contribution of gut metabolism in human health by spatially identifying the distribution of microbial metabolites. In comparison to previously applied approaches, NIMS with f-AuNPs provides high and, perhaps more importantly, heterogeneous coverage of multiple metabolite classes. This powerful tissue imaging technique can serve as a convenient platform for global and targeted exploration of the molecular makeup of the system with high sensitivity and lateral resolution.

Metabolic Organization of the Mouse Colon and Comparative Analysis of Diet-Related Rearrangements. Low matrix interference and high reproducibility are essential factors for comparative analysis of MSI data. However, MSI experiments based on previously reported approaches (*e.g.*, MALDI) usually provide poor reproducibility and high interference in the low molecular m/z range. Here we evaluated the suitability of NIMS with f-AuNPs for comparative global MSI studies by elucidating the metabolic variations occurring in the mouse colon under different dietary conditions. The study design involved nine mice fed with three different diets: a standard control diet (SD), a fiber deficient diet (FDD), and a polysaccharide and fiber deficient diet (PFD) (Figure 3A). Three biological replicates were collected for each condition and 5 μm tissue slices were analyzed according to the presented MSI protocol (Figure 3B). For comparative analysis, metabolite intensities were normalized to the total ion current in each pixel in the spectra and phosphocholine was used as reference for tissue alignment.

First, we defined the overall metabolic organization of the mouse colon under the SD diet regimen. Detected metabolites were divided according to relevant metabolic classes. Each class was determined by the sum of the normalized intensity values for representative molecules and their adducts (identified using an in-house R script to match with the METIN database within a 5 ppm error window). As shown in Figure 5A, the colon lumen contains high levels of lipid metabolites, which are of particularly high intensity in the center of the lumen, whereas bile acids appear uniformly distributed across the lumen as well as the colon mucosal and epithelial layers. Bile acids are endogenous molecules synthesized from cholesterol and further modified by gut bacteria.[62] Our approach detected primary (*e.g.*, cholic acid and muricholic acid as $[M + H]^+$, $[M + K]^+$ and $[M + H - H_2O]^+$, and chenodeoxycholic acid as $[M + H]^+$ and $[M + K]^+$), and conjugated bile acids (*e.g.*, taurolithocholic acid 3-sulfate as $[M + H]^+$). Primary bile acids are converted enzymatically to secondary bile acids *via* 7-dehydroxylation performed by the metabolic machinery of the gut microbiota.[63] For instance, we detected isomers of lithocholic acid and isolithocholic acid as $[M + H]^+$ and $[M + K]^+$, and deoxycholic acid as $[M + H]^+$ and $[M + K]^+$ (Table S1). Bile acids have both lipophilic and hydrophilic properties and are secreted into the duodenum to facilitate the absorption of lipids and lipo-soluble vitamins. Due to this amphipathic nature, bile acids act as emulsifiers and can therefore distribute evenly between the gut epithelia/mucosa and the lumen, as demonstrated in Figure 5B.

The overall distribution of metabolites involved in carbohydrate metabolism appears uniform in the colon

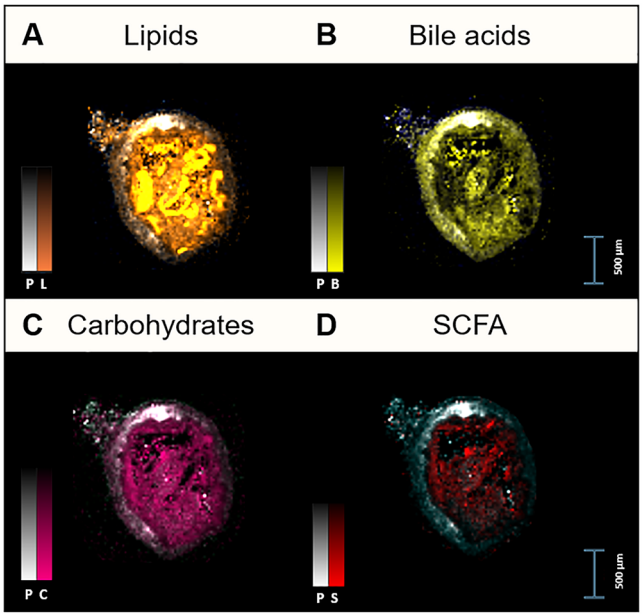

Figure 5. Overall metabolic organization of the mouse colon under standard diet: (A) lipids, (B) bile acids, (C) carbohydrates, (D) SCFA. Metabolite intensities were normalized according to the total ion signal in each pixel and reported as sum of intensities for each metabolic class. Phosphocholine was used for tissue alignment.

lumen and epithelia, with slightly higher relative content in the lumen (Figure 5C). Interestingly, the host-mouse does not possess the enzymatic capability to digest plant fibers and cellulose. However, the mouse gut harbors more than 500 bacterial species, including obligate and facultative anaerobes, that possess a wide repertoire of fiber- and cellulose-degrading enzymes[64] (*e.g.*, *Firmicutes*, *Bacteroidetes*, *Actinobacteria*, *Proteobacteria*, and *Verrucomicrobia*).[64−67] Consequently, the presence of carbohydrate metabolites in the lumen is likely mostly due to bacterial breakdown of dietary polysaccharides and fibers. Moreover, microbial communities in the colon are crucial to nondigestible carbohydrate/fiber fermentation, which results in the formation of short chain fatty acids (SCFA) (*e.g.*, acetate, propionate, butyrate). SCFA can be assimilated and used by the host, or function locally as signaling molecules involved in intestinal and immune homeostasis.[68,69] Consistent with this, we detected the presence of SCFA in the colon lumen (Figure 5D).

To explore the metabolic variations occurring in the mouse colon under different diets, we assessed the distribution of each metabolic class as obtained by the sum of the single normalized metabolite intensities (Figure 6). The carbohydrate content in both the PFD and FDD conditions are significantly ($p < 0.01$) reduced (averaged sum of normalized intensities difference >30%) compared to the SD. The lack of fiber in the FDD and PFD samples also results in a significant reduction of SCFA. These observations may highlight the occurrence of metabolic rearrangements in the mouse colon which similarly affect fiber and polysaccharide breakdown/utilization as well as the production of microbial fermentation end-products. The absence of fiber or polysaccharides in the mouse diet also induces a significant decrease in lipids, resulting in an even layer between the lumen and the mucosa (Figure 6). This difference is mostly due to a decrease in linoleic acid and/or related isobars, which appear to accumulate in the lumen

DOI: 10.1021/acsnano.8b02376
ACS Nano 2018, 12, 6938−6948

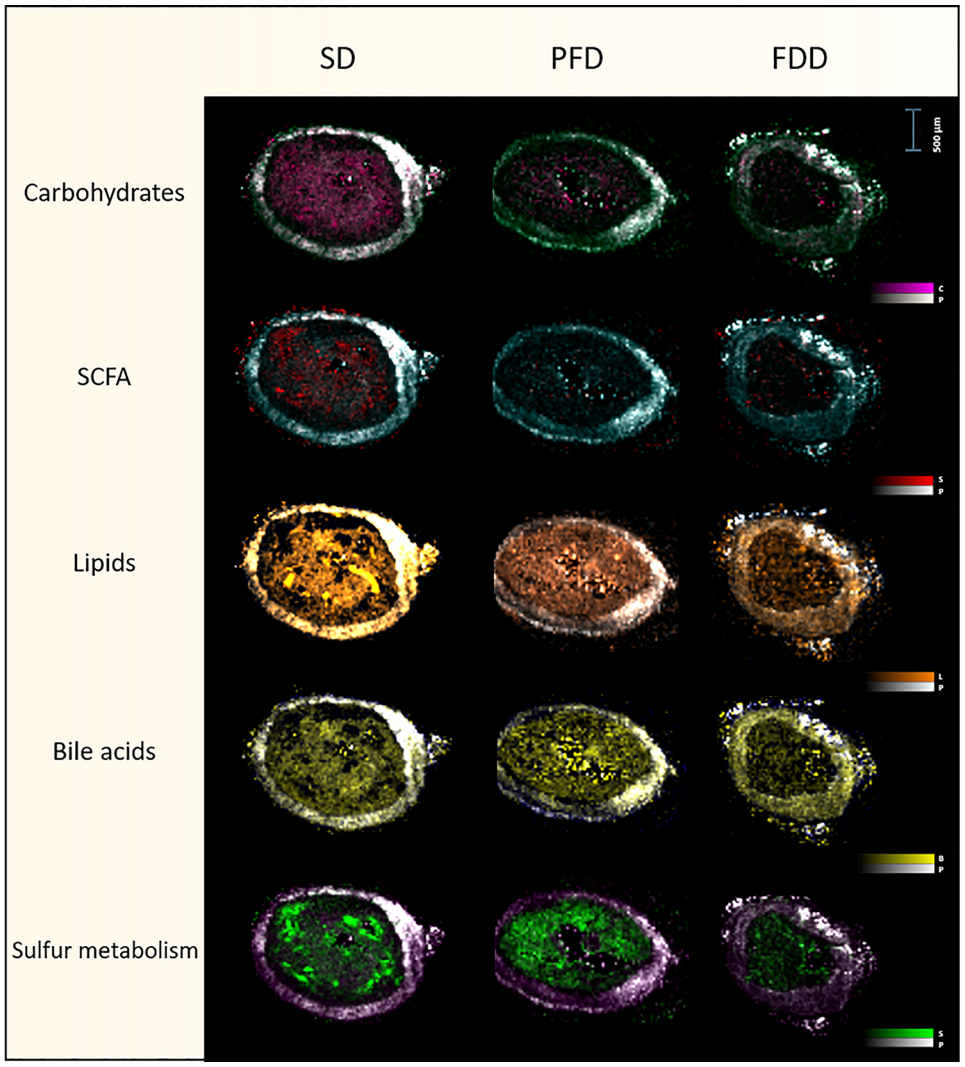

Figure 6. Metabolic rearrangement of the mouse colon under different diet regimen [standard diet (SD), fiber depleted diet (FDD) or polysaccharides and fiber depleted diet (PFD)]. Metabolite intensities were normalized according to the total ion signal in each pixel and reported as sum of intensities for each metabolic class. Phosphocholine was used for tissue alignment.

center (Figure S4). Of note, the detected bile acids are only slightly affected by different diet regimens, which may indicate that the diet does not affect gut microbial regulation of bile acid production. We also revealed large presence of sulfur metabolites in the SD regimen, and their substantial decrease under FDD, and, to a lesser extent ($p < 0.01$, averaged sum of normalized intensities difference <30%), under the PFD (Figure 6). In this case, the difference is linked to a decrease in sulfate intensity (SD *vs* FDD) and/or distribution (SD *vs* FDD and SD *vs* PFD) (Figure 6 and Figure S5). Gut microbes play a major role in the metabolism of sulfur in the colon lumen[70] as they can reduce sulfate while oxidizing organic compounds. Gut microbiota rearrangements involving sulfate-reducing bacteria, or increased degradation of the colonic mucus barrier resulting in enhanced sulfate release by mucinolytic bacteria,[71] may be at the basis of this observation.

Much is still unknown about the role of the gut microbiota in the digestion of dietary polysaccharides and fibers,[72] although several recent studies point to its key functional contribution and interaction with host metabolism. In particular, some commensal bacteria have adapted to switch between multiple different substrates, while others exhibit more selective behavior.[73] For example, *Ruminococcus flavefaciens* and *Fibrobacter succinogens* can degrade polysaccharides and cellulose and members of the genus *Bacteroides* can break down a wide range of plant polysaccharides. Interpreted in this scenario, our data point to the occurrence of important microbiome remodeling in the mice colon driven by the absence of dietary fibers or polysaccharides. These rearrangements may ultimately reflect in the spatial organization of intestinal metabolism, as here unraveled on the micrometer scale by using NIMS with f-AuNPs for comprehensive metabolome profiling in space.

CONCLUSIONS

NIMS with f-AuNPs leverages nanostructured gold surfaces functionalized with perfluorinated alkanes to facilitate the detection of small molecules by LDI mass spectrometry. This approach assists in the ablation process and can catalyze the D/I of metabolites directly from the surface of the sample, with minimal noise from the nanoparticles. This results in an increase in D/I efficiency accompanied by a decrease in the energy required for desorption. The use of perfluorohexane to distribute the f-AuNPs also creates a nonadherent environment

DOI: 10.1021/acsnano.8b02376
ACS Nano 2018, 12, 6938−6948

which remains homogeneous and separate from the hydrophilic surface of the sample, permitting MSI metabolomics experiments at a lateral resolution only limited by the diameter of the laser. Comparing with previous NIMS protocols for MSI, NIMS with functionalized gold nanoparticles does not involve the use of HF or other highly hazardous chemicals, thus facilitating the translation of the approach to the laboratory routine.

When applied to the comparative exploration of the mouse colon, our approach allowed for the direct detection of more than 1000 features, of which approximately 80 metabolites were consistently annotated among biological replicates. F-AuNPs provided heterogeneous metabolome coverage, including chemically diverse small molecules of both animal and microbial origin. Moreover, the approach unraveled significant rearrangements in the metabolic organization of the mouse colon, stimulated by a fiber and/or polysaccharide depleted diet. In particular, the decrease in carbohydrate, SCFA, lipid and sulfate in the polysaccharide and/or fiber depleted diets may be linked to variations in the relative composition of the colon microbiota.

In summary, the versatility of f-AuNPs NIMS can provide a comprehensive view on the distribution of metabolites in biological samples. We believe that this approach can offer a means to gain a mechanistic understanding from functional comparative MSI metabolomic studies. Our current and future efforts are in the direction of interfacing f-AuNPs NIMS with LDI sources with optimized laser focusing geometry,[2] and with ion beam cluster ion sources (*e.g.*, Bi_3^+ cluster ion source) to explore the potential of this technology for the detection of metabolites localization at the single cell level.

METHODS

Nanoparticles Synthesis. F-AuNPs were synthesized as previously described.[36] Briefly, 1 mL of 2% (v/v) octanethiol functionalized gold nanoparticles (2−4 nm diameter, 20 mg/mL in toluene, Sigma, Milwaukee, WI) were washed with 20 mL neat ethanol, followed by 20 mL acetone, sonicated for 1 min and centrifuged for 20 min at 3000 rpm between each wash. The washing steps were repeated three times. After removal of the supernatant, 1 mL hexane was added to the gold nanoparticles. The solution was tested for the presence of tetraoctyl ammonium ions (466 m/z), which can contaminate commercially available octanethiol functionalized gold nanoparticles. Next, 200 μL of 1*H*,1*H*,2*H*,2*H*-perfluorodecanethiol was added under N_2 flow and the resulting solution stirred for 72 h with a magnetic stir bar in a capped 30 mL glass vial. Glass is necessary to prevent contamination of nanoparticles for high resolution mass spectrometric measurements. After the reaction was complete, the solvent was evaporated under N_2 flow and the f-AuNPs were washed with hexane (three times), acetone (three times), and 1/1/1 methanol/acetone/water (two times). The particles were sonicated for 30 s and centrifugated at 3000 rpm at 4 °C between each wash. The supernatant was removed and the nanoparticles were dried at 90 °C in the oven and stored. A solution of f-AuNPs in PFH (3 mg/mL) was prepared and tested for contaminants before use. The f-AuNPs in PFH were stored in glass vials at room temperature until use.

Mass Spectrometric Conditions. Metabolites were detected using a Waters Synapt G2-Si quadrupole time-of-flight (Q-TOF) mass spectrometer equipped with a MALDI source (Waters, Milford, MA). HDImaging v1.4 and MassLynx v4.2 software, were used for data acquisition. Tissue samples were imaged with a 30 μm step size using a solid state Nd:YAG laser operating at 355 nm (laser energy 175, sampling rate 3 s, and repetition rate of 2500 Hz). Untargeted measurements were performed in resolution MS mode, in the 25−700 m/z range in positive mode. Calibration was performed prior analysis using red phosphorus clusters as a reference standard, and during spectra acquisition using tryptophan (205.0105 m/z) as internal lock mass. The nanoscaping data (Figure S2), obtained from cell extracts, were acquired on a Bruker Microflex MALDI-TOF MS with the MSP Biotarget adapter (Bruker Daltonics, Billerica, MA) at 35% laser power.

Metabolite identification was based on the accurate mass of the molecule matched against the METLIN database, observed isotope pattern and presence of related adducts at consistent spatial distribution. MS/MS experiments were performed to confirm metabolite identities when possible.

***In Vivo* Study.** Mice colon samples were obtained in the frame of a study investigating the spatial architecture of the mice colon. The study obtained the approval by the relevant institutional ethics committee and was conducted in accordance with the protocols approved by the Austrian laws (BMWF-66.006/0032-WF/V/3*b*/2014). In brief, mice were housed 12 h/12 h day/night cycle in a controlled environment, providing free access to food and water. Nine wild-type C57BL/6 mice maintained on a standard diet (R/M-H Ssniff, Germany) were divided in three groups (n = 3 per group) and fed for 1 week under a standard control diet (SD), a fiber-deficient diet (FDD), or a polysaccharide- and fiber-deficient diet (PFD) (Ssniff, Germany). Mice were sacrificed on day 7, and the colon was cryopreserved in optimal cutting material (OCT, Thermo Scientific, USA) and samples stored at −80 °C until analysis. Mouse brain tissues for SEM analysis were obtained in compliance with the National Institutes of Health and institutional guidelines (TSRI, International accredited). CB17-PrkdcSCID mice were euthanized by overdose of isoflurane. Mouse brain tissues were cryopreserved in OCT and samples stored at −80 °C until analysis.

Cell Extracts. *Bacteroides fragilis* cell extracts were kindly donated by the Forest Rohwer's lab, at San Diego State University. Briefly, cells were grown in brain heart infusion (BHI) media until 0.8 OD600 and then centrifuged at 13 000 rpm and 4 °C, the supernatant was removed, and cells were washed twice in minimal media and flash frozen in liquid nitrogen.

Sample Preparation. The frozen tissue samples were embedded in OCT and cryosectioned to obtain tissue slices (5 μm thickness) using a Leica 1900 cryostat (Buffalo Glove, IL). During this step attention should be posed to avoid any contact between the OCT material and the surface of the sample (*i.e.*, *via* the cutting blade), since some OCT component may contaminate the surface of the sample and contribute to the MS background noise. The slices were thaw-mounted on a piranha etched p-type silicon chip and the f-AuNPs solution in PFH (3 mg/mL) was topically distributed on the surface of the sample. Standard solutions of analytes were also prepared, deposited on the piranha etched p-type silicon chip, evaporated and covered with the f-AuNPs solution in PFH. Each chip was kept under vacuum at room temperature until analysis. *Bacteroides fragilis* cells were resuspended in 2/2/1 acetonitrile/methanol/water and underwent three freeze/thaw cycles in liquid nitrogen/ice cold water bath. After centrifugation the supernatant was evaporated and resuspended in 1/1 acetonitrile/water. The Dowex 200−400 mesh anionic resin particles (BioRad, Richmond, CA) were suspended in 1/1 acetonitrile/water (1 mg/mL). After mixing with the Dowex resin, samples were spotted (1 μL) and dried on the plate for MS analysis.

Transmission Electron Microscopy. F-AuNPs were deposited on 400 mesh copper grids and characterized by a Philips CM100 electron microscope (FEI, Hillsborough, OR) at 80 kV before and after irradiation (355 nm, laser energy 6.6 mJ, 2000 shots). Images were collected using a Megaview III CCD camera (Olympus Soft Imaging Solutions, Munster, Germany).

Scanning Electron Microscopy. SEM analysis were obtained with a Hitachi S4800 SEM at 5 kV. f-AuNPs were distributed on the surface of a clean piranha etched p-type silicon chip or one drop of the f-AuNPs solution in PFH (3 mg/mL) was topically distributed on the surface of a tissue slice. PFH was dried under vacuum at room temperature and the sample irradiated by a MALDI source with a laser with a 250 μm step size (included in the AB SCIEX TOF/TOF 5800 MS system).

DOI: 10.1021/acsnano.8b02376
ACS Nano 2018, 12, 6938−6948

Data Analysis. Data analysis was performed in HDImaging v1.4 software (Waters, Milford, MA), also used to preprocess and normalize metabolite intensities. Statistical analysis was performed on normalized ion intensities for each metabolic class between different diet conditions (two sided *t* test, assuming unequal variance distribution). The significance threshold was set at $p < 0.01$. Metabolite abundances were considered different for statistically significant ($p < 0.01$) variations >30% (averaged intensity), as semiquantitative estimation of the variation. The obtained data sets were putatively annotated against the METLIN database based on a mass deviation of 5 ppm using an in-house R script. MS/MS data were processed in MassLynx v4.2 software. Data analysis was performed in the KNIME Analytics Platform (Konstanz, Germany).

ASSOCIATED CONTENT

Supporting Information

The Supporting Information is available free of charge on the ACS Publications website at DOI: 10.1021/acsnano.8b02376.

List of detected metabolites, supporting figures for metabolome coverage, metabolites dislocation and OCT distribution, mass spectra for the combined use of f-AuNPs with the Dowex resin, distribution of targeted metabolites dysregulated under different diets in mice colon (PDF)

Table S1 (XLSX)

AUTHOR INFORMATION

Corresponding Author

*E-mail: siuzdak@scripps.edu.

ORCID

Amelia Palermo: 0000-0001-5705-6521

Erica M. Forsberg: 0000-0001-5190-1501

Benedikt Warth: 0000-0002-6104-0706

Gary Siuzdak: 0000-0002-4749-0014

Author Contributions

#A.P. and E.M.F. contributed equally.

Notes

The authors declare no competing financial interest.

ACKNOWLEDGMENTS

This research was partially funded by Ecosystems and Networks Integrated with Genes and Molecular Assemblies (ENIGMA), a Scientific Focus Area Program at Lawrence Berkeley National Laboratory for the US Department of Energy, Office of Science, Office of Biological and Environmental Research under contract number DE-AC02-05CH11231 (G.S.); and National Institutes of Health grants R01 GM114368-03, P30 MH062261-10, and P01 DA026146-02 (G.S.).

REFERENCES

(1) Buchberger, A. R.; DeLaney, K.; Johnson, J.; Li, L. Mass Spectrometry Imaging: A Review of Emerging Advancements and Future Insights. *Anal. Chem.* **2018**, *90*, 240−265.

(2) Kompauer, M.; Heiles, S.; Spengler, B. Atmospheric Pressure MALDI Mass Spectrometry Imaging of Tissues and Cells at 1.4-Mum Lateral Resolution. *Nat. Methods* **2017**, *14*, 90−96.

(3) Ly, A.; Buck, A.; Balluff, B.; Sun, N.; Gorzolka, K.; Feuchtinger, A.; Janssen, K. P.; Kuppen, P. J. K.; Van De Velde, C. J. H.; Weirich, G.; Erlmeier, F.; Langer, R.; Aubele, M.; Zitzelsberger, H.; McDonnell, L.; Aichler, M.; Walch, A. High-Mass-Resolution MALDI Mass Spectrometry Imaging of Metabolites from Formalin-Fixed Paraffin-Embedded Tissue. *Nat. Protoc.* **2016**, *11*, 1428−1443.

(4) Sturtevant, D.; Lee, Y. J.; Chapman, K. D. Matrix Assisted Laser Desorption/Ionization-Mass Spectrometry Imaging (MALDI-MSI) for Direct Visualization of Plant Metabolites *in Situ*. *Curr. Opin. Biotechnol.* **2016**, *37*, 53−60.

(5) Vickerman, J. C. Molecular Imaging and Depth Profiling by Mass Spectrometry—SIMS, MALDI or DESI? *Analyst* **2011**, *136*, 2199−2217.

(6) Aichler, M.; Walch, A. MALDI Imaging Mass Spectrometry: Current Frontiers and Perspectives in Pathology Research and Practice. *Lab. Invest.* **2015**, *95*, 422−431.

(7) Mirabelli, M. F.; Zenobi, R. Observing Proton Transfer Reactions Inside the MALDI Plume: Experimental and Theoretical Insight into MALDI Gas-Phase Reactions. *J. Am. Soc. Mass Spectrom.* **2017**, *28*, 1676−1686.

(8) Zenobi, R.; Knochenmuss, R. Ion Formation in MALDI Mass Spectrometry. *Mass Spectrom. Rev.* **1998**, *17*, 337−366.

(9) Etalo, D.; de Vos, R. C.; Joosten, M. H. A. J.; Hall, R. Spatially-Resolved Plant Metabolomics: Some Potentials and Limitations of Laser-Ablation Electrospray Ionization (LAESI) Mass Spectrometry Metabolite Imaging. *Plant Physiol.* **2015**, *169*, 1424−1435.

(10) Bontha, S. V.; Maluf, D. G.; Mueller, T. F.; Mas, V. R. Systems Biology in Kidney Transplantation: The Application of Multi-Omics to a Complex Model. *Am. J. Transplant.* **2017**, *17*, 11−21.

(11) Hood, L.; Heath, J. R.; Phelps, M. E.; Lin, B. Systems Biology and New Technologies Enable Predictive and Preventative Medicine. *Science* **2004**, *306*, 640−643.

(12) Jackson, S. N.; Woods, A. S. The Development of Matrix-Assisted Laser Desorption Ionization (MALDI) Mass Spectrometry. *In The Encyclopedia of Mass Spectrometry* **2016**, 124−131.

(13) Shi, R.; Dai, X.; Li, W.; Lu, F.; Liu, Y.; Qu, H.; Li, H.; Chen, Q.; Tian, H.; Wu, E.; Wang, Y.; Zhou, R.; Lee, S.; Lifshitz, Y.; Kang, Z.; Liu, J. Hydroxyl-Group-Dominated Graphite Dots Reshape Laser Desorption/Ionization Mass Spectrometry for Small Biomolecular Analysis and Imaging. *ACS Nano* **2017**, *11*, 9500−9513.

(14) Shroff, R.; Rulísek, L.; Doubsky, J.; Svatos, A. Acid-Base-Driven Matrix-Assisted Mass Spectrometry for Targeted Metabolomics. *Proc. Natl. Acad. Sci. U. S. A.* **2009**, *106*, 10092−10096.

(15) Yang, J.; Caprioli, R. M. Matrix Sublimation/Recrystallization for Imaging Proteins by Mass Spectrometry at High Spatial Resolution. *Anal. Chem.* **2011**, *83*, 5728−5734.

(16) Holzlechner, M.; Reitschmidt, S.; Gruber, S.; Zeilinger, S.; Marchetti-Deschmann, M. Visualizing Fungal Metabolites during Mycoparasitic Interaction by MALDI Mass Spectrometry Imaging. *Proteomics* **2016**, *16*, 1742−1746.

(17) Nemes, P.; Vertes, A. Laser Ablation Electrospray Ionization for Atmospheric Pressure, *in Vivo*, and Imaging Mass Spectrometry. *Anal. Chem.* **2007**, *79*, 8098−8106.

(18) Northen, T. R.; Yanes, O.; Northen, M. T.; Marrinucci, D.; Uritboonthai, W.; Apon, J.; Golledge, S. L.; Nordström, A.; Siuzdak, G. Clathrate Nanostructures for Mass Spectrometry. *Nature* **2007**, *449*, 1033−1036.

(19) Winograd, N. The Magic of Cluster SIMS. *Anal. Chem.* **2005**, *77*, 142A−149A.

(20) Winograd, N. Imaging Mass Spectrometry on the Nanoscale with Cluster Ion Beams. *Anal. Chem.* **2015**, *87*, 328−333.

(21) Kraft, M. L.; Weber, P. K.; Longo, M. L.; Hutcheon, I. D.; Boxer, S. G. Phase Separation of Lipid Membranes Analyzed with High-Resolution Secondary Ion Mass Spectrometry. *Science* **2006**, *313*, 1948−1951.

(22) Weibel, D. E.; Lockyer, N.; Vickerman, J. C. C60 Cluster Ion Bombardment of Organic Surfaces. *Appl. Surf. Sci.* **2004**, *231*, 146−152.

(23) Ostrowski, S. G.; Szakal, C.; Kozole, J.; Roddy, T. P.; Xu, J.; Ewing, A. G.; Winograd, N. Secondary Ion MS Imaging of Lipids in Picoliter Vials with a Buckminsterfullerene Ion Source. *Anal. Chem.* **2005**, *77*, 6190−6196.

(24) Passarelli, M. K.; Newman, C. F.; Marshall, P. S.; West, A.; Gilmore, I. S.; Bunch, J.; Alexander, M. R.; Dollery, C. T. Single-Cell Analysis: Visualizing Pharmaceutical and Metabolite Uptake in Cells

DOI: 10.1021/acsnano.8b02376
ACS Nano 2018, 12, 6938−6948

with Label-Free 3D Mass Spectrometry Imaging. *Anal. Chem.* **2015**, *87*, 6696−6702.
(25) Passarelli, M. K.; Ewing, A. G. Single-Cell Imaging Mass Spectrometry. *Curr. Opin. Chem. Biol.* **2013**, *17*, 854−859.
(26) Passarelli, M. K.; Pirkl, A.; Moellers, R.; Grinfeld, D.; Kollmer, F.; Havelund, R.; Newman, C. F.; Marshall, P. S.; Arlinghaus, H.; Alexander, M. R.; Dollery, C. T.; Gilmore, I. S. The 3D OrbiSIMS - Label-Free Metabolic Imaging with Subcellular Lateral Resolution and High Mass-Resolving Power. *Nat. Methods* **2017**, *14*, 1175.
(27) Venter, A.; Sojka, P. E.; Cooks, R. G. Droplet Dynamics and Ionization Mechanisms in Desorption Electrospray Ionization Mass Spectrometry. *Anal. Chem.* **2006**, *78*, 8549−8555.
(28) Takáts, Z.; Wiseman, J. M.; Gologan, B.; Cooks, R. G. Mass Spectrometry Sampling under Ambient Conditions with Desorption Electrospray Ionization. *Science* **2004**, *306*, 471−473.
(29) Watrous, J.; Roach, P.; Heath, B.; Alexandrov, T.; Laskin, J.; Dorrestein, P. C. Metabolic Profiling Directly from the Petri Dish Using Nanospray Desorption Electrospray Ionization Imaging Mass Spectrometry. *Anal. Chem.* **2013**, *85*, 10385−10391.
(30) Ray, A.; Bristow, T.; Whitmore, C.; Mosely, J. On-Line Reaction Monitoring by Mass Spectrometry, Modern Approaches for the Analysis of Chemical Reactions. *Mass Spectrom. Rev.* **2018**, *19*, 565.
(31) Tillner, J.; Wu, V.; Jones, E. A.; Pringle, S. D.; Karancsi, T.; Dannhorn, A.; Veselkov, K.; McKenzie, J. S.; Takats, Z. Faster, More Reproducible DESI-MS for Biological Tissue Imaging. *J. Am. Soc. Mass Spectrom.* **2017**, *28*, 2090−2098.
(32) Greving, M. P.; Patti, G. J.; Siuzdak, G. Nanostructure-Initiator Mass Spectrometry Metabolite Analysis and Imaging. *Anal. Chem.* **2011**, *83*, 2−7.
(33) Guinan, T. M.; Gustafsson, O. J. R.; McPhee, G.; Kobus, H.; Voelcker, N. H. Silver Coating for High-Mass-Accuracy Imaging Mass Spectrometry of Fingerprints on Nanostructured Silicon. *Anal. Chem.* **2015**, *87*, 11195−11202.
(34) Francese, S.; Bradshaw, R.; Denison, N. An Update on MALDI Mass Spectrometry Based Technology for the Analysis of Fingermarks − Stepping into Operational Deployment. *Analyst* **2017**, *142*, 2518−2546.
(35) Rocha, B.; Ruiz-Romero, C.; Blanco, F. J. Mass Spectrometry Imaging: A Novel Technology in Rheumatology. *Nat. Rev. Rheumatol.* **2017**, *13*, 52.
(36) Kurczy, M. E.; Zhu, Z. J.; Ivanisevic, J.; Schuyler, A. M.; Lalwani, K.; Santidrian, A. F.; David, J. M.; Giddabasappa, A.; Roberts, A. J.; Olivos, H. J.; O'Brien, P. J.; Franco, L.; Fields, M. W.; Paris, L. P.; Friedlander, M.; Johnson, C. H.; Epstein, A. A.; Gendelman, H. E.; Wood, M. R.; Felding, B. H.; et al. Comprehensive Bioimaging with Fluorinated Nanoparticles Using Breathable Liquids. *Nat. Commun.* **2015**, *6*, 5998.
(37) Picca, R. A.; Calvano, C. D.; Cioffi, N.; Palmisano, F. Mechanisms of Nanophase-Induced Desorption in LDI-MS. A Short Review. *Nanomaterials* **2017**, *7*, 75.
(38) Taira, S.; Sugiura, Y.; Moritake, S.; Shimma, S.; Ichiyanagi, Y.; Setou, M. Nanoparticle-Assisted Laser Desorption/Ionization Based Mass Imaging with Cellular Resolution. *Anal. Chem.* **2008**, *80*, 4761−4766.
(39) Kawasaki, H.; Yonezawa, T.; Watanabe, T.; Arakawa, R. Platinum Nanoflowers for Surface-Assisted Laser Desorption/Ionization Mass Spectrometry of Biomolecules. *J. Phys. Chem. C* **2007**, *111*, 16278−16283.
(40) Pilolli, R.; Palmisano, F.; Cioffi, N. Gold Nanomaterials as a New Tool for Bioanalytical Applications of Laser Desorption Ionization Mass Spectrometry. *Anal. Bioanal. Chem.* **2012**, *402*, 601−623.
(41) Lee, K. H.; Chiang, C. K.; Lin, Z. H.; Chang, H. T. Determining Enediol Compounds in Tea Using Surface-Assisted Laser Desorption/Ionization Mass Spectrometry with Titanium Dioxide Nanoparticle Matrices. *Rapid Commun. Mass Spectrom.* **2007**, *21*, 2023−2030.
(42) Silina, Y. E.; Fink-Straube, C.; Hayen, H.; Volmer, D. A. Analysis of Fatty Acids and Triacylglycerides by Pd Nanoparticle-Assisted Laser Desorption/Ionization Mass Spectrometry. *Anal. Methods* **2015**, *7*, 3701−3707.
(43) Dong, X.; Cheng, J.; Li, J.; Wang, Y. Graphene as a Novel Matrix for the Analysis of Small Molecules by MALDI-TOF MS. *Anal. Chem.* **2010**, *82*, 6208−6214.
(44) Go, E. P.; Apon, J. V.; Luo, G.; Saghatelian, A.; Daniels, R. H.; Sahi, V.; Dubrow, R.; Cravatt, B. F.; Vertes, A.; Siuzdak, G. Desorption/Ionization on Silicon Nanowires. *Anal. Chem.* **2005**, *77*, 1641−1646.
(45) Jain, P. K.; Lee, K. S.; El-Sayed, I. H.; El-Sayed, M. A. Calculated Absorption and Scattering Properties of Gold Nanoparticles of Different Size, Shape, and Composition: Applications in Biological Imaging and Biomedicine. *J. Phys. Chem. B* **2006**, *110*, 7238−7248.
(46) Tang, H. W.; Wong, M. Y.; Lam, W.; Cheng, Y. C.; Che, C. M.; Ng, K. M. Molecular Histology Analysis by Matrix-Assisted Laser Desorption/Ionization Imaging Mass Spectrometry Using Gold Nanoparticles as Matrix. *Rapid Commun. Mass Spectrom.* **2011**, *25*, 3690−3696.
(47) Su, C. L.; Tseng, W. L. Gold Nanoparticles as Assisted Matrix for Determining Neutral Small Carbohydrates through Laser Desorption/Ionization Time-of-Flight Mass Spectrometry. *Anal. Chem.* **2007**, *79*, 1626−1633.
(48) Huang, Y. F.; Chang, H. T. Nile Red-Adsorbed Gold Nanoparticle Matrixes for Determining Aminothiols through Surface-Assisted Laser Desorption/Ionization Mass Spectrometry. *Anal. Chem.* **2006**, *78*, 1485−1493.
(49) Wang, J.; Jie, M.; Li, H.; Lin, L.; He, Z.; Wang, S.; Lin, J. M. Gold Nanoparticles Modified Porous Silicon Chip for SALDI-MS Determination of Glutathione in Cells. *Talanta* **2017**, *168*, 222−229.
(50) Zhu, Z.-J.; Ghosh, P. S.; Miranda, O. R.; Vachet, R. W.; Rotello, V. M. Multiplexed Screening of Cellular Uptake of Gold Nanoparticles Using Laser Desorption/Ionization Mass Spectrometry. *J. Am. Chem. Soc.* **2008**, *130*, 14139−14143.
(51) Nicolardi, S.; Van Der Burgt, Y. E. M.; Codée, J. D. C.; Wuhrer, M.; Hokke, C. H.; Chiodo, F. Structural Characterization of Biofunctionalized Gold Nanoparticles by Ultrahigh-Resolution Mass Spectrometry. *ACS Nano* **2017**, *11*, 8257−8264.
(52) Zhou, J.; Ralston, J.; Sedev, R.; Beattie, D. A. Functionalized Gold Nanoparticles: Synthesis, Structure and Colloid Stability. *J. Colloid Interface Sci.* **2009**, *331*, 251−262.
(53) Woehrle, G. H.; Brown, L. O.; Hutchison, J. E. Thiol-Functionalized, 1.5-Nm Gold Nanoparticles through Ligand Exchange Reactions: Scope and Mechanism of Ligand Exchange. *J. Am. Chem. Soc.* **2005**, *127*, 2172−2183.
(54) Biffinger, J. C.; Kim, H. W.; DiMagno, S. G. The Polar Hydrophobicity of Fluorinated Compounds. *ChemBioChem* **2004**, *5*, 622−627.
(55) Cooper, D. L.; Allan, N. L.; Powell, R. L. Theoretical Studies of Fluorocarbons Part III. Primary, Secondary, Tertiary and Quaternary Centres. *J. Fluorine Chem.* **1990**, *49*, 421−432.
(56) Miura, D.; Fujimura, Y.; Wariishi, H. In Situ Metabolomic Mass Spectrometry Imaging: Recent Advances and Difficulties. *J. Proteomics* **2012**, *75*, 5052−5060.
(57) Smith, C. A.; O'Maille, G.; Want, E. J.; Qin, C.; Trauger, S. A.; Brandon, T. R.; Custodio, D. E.; Abagyan, R.; Siuzdak, G. METLIN: A Metabolite Mass Spectral Database. *Ther. Drug Monit.* **2005**, *27*, 747−751.
(58) DeBerardinis, R. J.; Mancuso, A.; Daikhin, E.; Nissim, I.; Yudkoff, M.; Wehrli, S.; Thompson, C. B. Beyond Aerobic Glycolysis: Transformed Cells Can Engage in Glutamine Metabolism That Exceeds the Requirement for Protein and Nucleotide Synthesis. *Proc. Natl. Acad. Sci. U. S. A.* **2007**, *104*, 19345−19350.
(59) Allen, E. L.; Ulanet, D. B.; Pirman, D.; Mahoney, C. E.; Coco, J.; Si, Y.; Chen, Y.; Huang, L.; Ren, J.; Choe, S.; Clasquin, M. F.; Artin, E.; Fan, Z. P.; Cianchetta, G.; Murtie, J.; Dorsch, M.; Jin, S.; Smolen, G. A. Differential Aspartate Usage Identifies a Subset of

DOI: 10.1021/acsnano.8b02376
ACS Nano 2018, 12, 6938−6948

Cancer Cells Particularly Dependent on OGDH. *Cell Rep.* **2016**, *17*, 876−890.
(60) Ke, H.; Lewis, I. A.; Morrisey, J. M.; McLean, K. J.; Ganesan, S. M.; Painter, H. J.; Mather, M. W.; Jacobs-Lorena, M.; Llinás, M.; Vaidya, A. B. Genetic Investigation of Tricarboxylic Acid Metabolism during the Plasmodium Falciparum Life Cycle. *Cell Rep.* **2015**, *11*, 164−174.
(61) Kaiko, G. E.; Ryu, S. H.; Koues, O. I.; Collins, P. L.; Solnica-Krezel, L.; Pearce, E. L.; Oltz, E. M.; Stappenbeck, T. S. The Colonic Crypt Protects Stem Cells from Microbiota-Derived Metabolites. *Cell* **2016**, *165*, 1−13.
(62) De Aguiar Vallim, T. Q.; Tarling, E. J.; Edwards, P. A. Pleiotropic Roles of Bile Acids in Metabolism. *Cell Metab.* **2013**, *17*, 657−669.
(63) Wahlström, A.; Sayin, S. I.; Marschall, H. U.; Bäckhed, F. Intestinal Crosstalk between Bile Acids and Microbiota and Its Impact on Host Metabolism. *Cell Metab.* **2016**, *24*, 41−50.
(64) Lupp, C.; Robertson, M. L.; Wickham, M. E.; Sekirov, I.; Champion, O. L.; Gaynor, E. C.; Finlay, B. B. Host-Mediated Inflammation Disrupts the Intestinal Microbiota and Promotes the Overgrowth of Enterobacteriaceae. *Cell Host Microbe* **2007**, *2*, 119−129.
(65) Murphy, E. F.; Cotter, P. D.; Healy, S.; Marques, T. M.; O'Sullivan, O.; Fouhy, F.; Clarke, S. F.; O'Toole, P. W.; Quigley, E. M.; Stanton, C.; Ross, P. R.; O'Doherty, R. M.; Shanahan, F. Composition and Energy Harvesting Capacity of the Gut Microbiota: Relationship to Diet, Obesity and Time in Mouse Models. *Gut* **2010**, *59*, 1635−1642.
(66) Bercik, P.; Denou, E.; Collins, J.; Jackson, W.; Lu, J.; Jury, J.; Deng, Y.; Blennerhassett, P.; MacRi, J.; McCoy, K. D.; Verdu, E. F.; Collins, S. M. The Intestinal Microbiota Affect Central Levels of Brain-Derived Neurotropic Factor and Behavior in Mice. *Gastroenterology* **2011**, *141*, 599−609.
(67) Benson, A. K.; Kelly, S. A.; Legge, R.; Ma, F.; Low, S. J.; Kim, J.; Zhang, M.; Oh, P. L.; Nehrenberg, D.; Hua, K.; Kachman, S. D.; Moriyama, E. N.; Walter, J.; Peterson, D. A.; Pomp, D. Individuality in Gut Microbiota Composition Is a Complex Polygenic Trait Shaped by Multiple Environmental and Host Genetic Factors. *Proc. Natl. Acad. Sci. U. S. A.* **2010**, *107*, 18933−18938.
(68) Morrison, D. J.; Preston, T. Formation of Short Chain Fatty Acids by the Gut Microbiota and Their Impact on Human Metabolism. *Gut Microbes* **2016**, *7*, 189−200.
(69) Ghazalpour, A.; Cespedes, I.; Bennett, B. J.; Allayee, H. Expanding Role of Gut Microbiota in Lipid Metabolism. *Curr. Opin. Lipidol.* **2016**, *27*, 141−147.
(70) Carbonero, F.; Benefiel, A. C.; Alizadeh-Ghamsari, A. H.; Gaskins, H. R. Microbial Pathways in Colonic Sulfur Metabolism and Links with Health and Disease. *Front. Physiol.* **2012**, *3*, 448.
(71) Desai, M. S.; Seekatz, A. M.; Koropatkin, N. M.; Kamada, N.; Hickey, C. A.; Wolter, M.; Pudlo, N. A.; Kitamoto, S.; Terrapon, N.; Muller, A.; Young, V. B.; Henrissat, B.; Wilmes, P.; Stappenbeck, T. S.; Núñez, G.; Martens, E. C. A Dietary Fiber-Deprived Gut Microbiota Degrades the Colonic Mucus Barrier and Enhances Pathogen Susceptibility. *Cell* **2016**, *167*, 1339−1353.
(72) Flint, H. J.; Bayer, E. A.; Rincon, M. T.; Lamed, R.; White, B. A. Polysaccharide Utilization by Gut Bacteria: Potential for New Insights from Genomic Analysis. *Nat. Rev. Microbiol.* **2008**, *6*, 121−131.
(73) McWilliam Leitch, E. C.; Walker, A. W.; Duncan, S. H.; Holtrop, G.; Flint, H. J. Selective Colonization of Insoluble Substrates by Human Faecal Bacteria. *Environ. Microbiol.* **2006**, *72*, 667−679.

DOI: 10.1021/acsnano.8b02376
ACS Nano 2018, 12, 6938−6948